ISSN No:-2456-2165 https://doi.org/10.38124/ijisrt/26sep319

Design and Performance Evaluation of an On-Board Pulsed-DC Resonance Electrolyzer for Hydrogen-Biased Electric Powertrains

Kishan Ranoliya[1]; Dr. S. B. Shah[2]

[1]Student of Mechanical Engineering at L. D. College of Engineering (GTU)
[2]Assistant Professor of Mechanical Engineering at L. D. College of Engineering (GTU)

Publication Date: 2026/09/16

Abstract: The development of sustainable energy carriers that get around the infrastructure issues with high-pressure hydrogen storage is essential for the shift to zero-emission mobility. In order to avoid the dangers associated with high-pressure hydrogen storage, this research assesses an on-board "water-to-hydrogen" cycle for hybrid electric vehicles. The process of producing hydrogen depends on a 555-timer-controlled MOSFET circuit that supplies a water capacitor cell with high-voltage pulsed-DC resonance via a toroidal bifilar transformer. According to stoichiometry, 10L of water produce 1.11kg of H_2 and 8.88kg of O_2 (43.77kWh HHV). It provides the traction motor with ~22kWh of net energy after passing through a 1kW PEM fuel cell at 50% efficiency. Additionally examined are key changes to internal combustion engines, such as flashback arrestors, cooler spark plugs, and delayed ignition. On-board resonance generation provides a feasible localized storage option that complies with thermodynamic rules.

Keywords: *Hydrogen-Biased Vehicle; Pulsed-DC Electrolysis; Resonant Charging Choke; PEM Fuel Cell; Hydrogen ICE; Thermodynamic Efficiency.*

How to Cite: Kishan Ranoliya; Dr. S. B. Shah (2026) Design and Performance Evaluation of an On-Board Pulsed-DC Resonance Electrolyzer for Hydrogen-Biased Electric Powertrains. *International Journal of Innovative Science and Research Technology,* 11(9), 225-231. https://doi.org/10.38124/ijisrt/26sep319

I. INTRODUCTION

The global automotive industry is facing unprecedented pressure to decarbonize due to tightening emission regulations and the depletion of fossil fuel reserves [1]. While battery electric vehicles (BEVs) have seen widespread adoption, their long-term viability remains constrained by lithium-ion resource scarcity, long charging intervals, and significant grid degradation during peak demands [2]. Consequently, hydrogen (H_2) has emerged as a premier alternative fuel owing to its high specific energy density and zero-carbon emission profile at the point of use [3].

However, the logistics of storage and distribution significantly impede the widespread deployment of hydrogen fuel cell vehicles (FCEVs). Standard vehicular hydrogen storage requires gaseous compression at extreme pressures—typically 350 to 700 bar—demanding complex, multi-layered composite tanks and highly specialized station infrastructure [4]; [5]. Furthermore, the safety risks associated with high-pressure gas storage in passenger vehicles present significant consumer anxieties and engineering challenges regarding impact resistance and thermal management during fast fuelling cycles.

To bypass these infrastructure liabilities, researchers have recently explored the paradigm of on-board hydrogen generation, wherein water acts as a stable, non-hazardous energy carrier molecule rather than a direct fuel source [1]. Conventional continuous direct-current (DC) electrolysis, however, features low Faraday efficiency when scaled down to vehicular dimensions due to significant thermal losses, overpotential barriers, and rapid electrode degradation [6]. To counteract these inefficiencies, this research focuses on the deployment of an optimized pulsed-DC high-frequency resonance electrolysis system. By matching the electrical excitation frequency to the inherent dielectric resonance properties of the fluid matrix, the overpotential required to trigger molecular cleavage can be minimized, enhancing the net gas yield per unit of electrical input.

This manuscript details the comprehensive design, simulation, and experimental execution of a hydrogen-biased vehicle powertrain. The structural architecture includes an advanced pulse generation circuit operating at 22.4 Kilohertz, an on-board light-weight composite gas buffer tank utilizing plastic, carbon fibre, and glass fibre laminates, and a dual-application energy conversion analysis evaluating both a 1 kW Proton Exchange Membrane (PEM) fuel cell stack and a modified Internal Combustion Engine (ICE) platform.

ISSN No:-2456-2165 https://doi.org/10.38124/ijisrt/26sep319

Through meticulous mathematical modelling and empirical testing, the efficiency limits and operational characteristics of this closed-loop powertrain are characterized to provide a framework for future zero-emission vehicular designs.

II. MATHEMATICAL AND THERMODYNAMIC FRAMEWORK

To validate the scalability and operational efficiency of the on-board hydrogen generation system, a robust mathematical model must govern the electrical excitation circuit and the physical storage parameters of the generated gas [1]. This section establishes the theoretical foundations controlling the high-frequency pulsed-DC resonance and characterizes the compression thermodynamics within the multi-layered composite storage assembly.

➢ *Pulsed-DC Frequency and Duty Cycle Derivation*

The electrical fragmentation of the water molecule matrix is heavily dependent on the output frequency of the pulse generation circuit. By utilizing an astable NE555 timer architecture configured with asymmetric charging paths via steering diodes, the output frequency (f) and duty cycle (D) can be precisely tuned using fixed resistor R_A, potentiometer R_B, and timing capacitor C.

The total charging time (t_1, output high) occurs as current passes through R_A and the forward-biased portion of R_B to charge the capacitor C:

$$t_1 = 0.693 \cdot (R_A + R_{B1}) \cdot C$$

The discharging time (t_2, output low) occurs as the capacitor evacuates its stored charge through the remaining resistance of the potentiometer R_{B2} directly into the discharge pin (Pin 7) of the IC:

$$t_2 = 0.693 \cdot R_{B2} \cdot C$$

Assuming a balanced potentiometer distribution where the total active resistance is expressed as R_B, the total periodic oscillation time (T) equals the summation of both intervals:

$$T = t_1 + t_2 = 0.693 \cdot (R_A + 2R_B) \cdot C$$

The fundamental operating frequency (f) of the pulse generator is the mathematical inverse of the period T, which aligns with the empirical circuit configurations established in this design:

$$f = \frac{1}{T} = \frac{1.44}{(R_A + 2R_B) \cdot C}$$

Given the hardware constraints defined in the experimental setup ($R_A = 1\ \text{k}\Omega$, $R_B = 10\ \text{k}\Omega$ potentiometer, and a high-frequency ceramic capacitor $C = 2.9\ \text{nF}$), the resulting target resonance frequency is evaluated as:

$$f = \frac{1.44}{\big(1000 + 2(10000)\big) \cdot 2.9 \times 10^{-9}} \approx 23{,}645\ \text{Hz}$$

This derived value approximates the 22.4 Kilohertz target frequency used during electrical simulation. The slight variance accounts for nominal component tolerances and internal propagation delays within the NE555 silicon matrix.

➢ *Real Gas Thermodynamics at Pressure (20 bar)*

While on-board hydrogen generation significantly diminishes the volume of explosive volatile gases stored at any single moment, localized transient buffering requires structural storage containment up to peak pressure of 20 bar. At such pressures, hydrogen deviates radically from ideal gas behaviours due to the finite volume occupied by the molecules themselves and the weak intermolecular forces acting under close confinement. Consequently, the standard Ideal Gas Law introduces severe calculation errors, necessitating the application of the Compressibility Factor (Z) modification within the real gas equation of state [7]:

$$P \cdot V = Z \cdot n \cdot R \cdot T$$

Where:

- P = System absolute pressure (20×10^5 Pa)
- V = Geometric volume of the internal cylinder capsule (m^3)
- Z = Compressibility factor (≈ 1.09 for H_2 at 20 bar and 298.15 K)
- n = Molar mass quantity of stored hydrogen (moles)
- R = Universal gas constant ($8.3144\ \text{J}/(\text{mol} \cdot \text{K})$)
- T = Surrounding ambient temperature thermal baseline (298.15 K)

To determine the compressibility factor (Z) with precision across varying operational boundaries, the van der Waals equation of state is applied to isolate the specific molar volume ($v_m = V/n$) [8]:

$$\left(P + \frac{a}{v_m^2}\right)(v_m - b) = R \cdot T$$

For pure hydrogen gas, the highly isolated critical parameters define the empirical constants as:

- $a = 0.02476\ \text{Pa} \cdot \text{m}^6/\text{mol}^2$ (attraction coefficient)
- $b = 2.661 \times 10^{-5}\ \text{m}^3/\text{mol}$ (effective molecular co-volume)

Solving this cubic equation for v_m under 20 bar conditions yields a heavily reduced available space layout, resulting in a calculated Z value of:

$$Z = \frac{P \cdot v_m}{R \cdot T} \approx 1.09$$

➢ *Multi-Layered Laminate Wall Stress and Thermal Capacity*

The composite tank consists of three distinct concentric layers: an inner Plastic liner, a middle Carbon Fiber structural shell, and an outer Glass Fiber protective envelope. The structural resilience against internal real gas pressure P is

ISSN No:-2456-2165 https://doi.org/10.38124/ijisrt/26sep319

determined using thick-walled pressure vessel mechanics defined by Lamé's equations. The total radial wall thickness (t_{total}) is the summation of individual laminate layers:

$$t_{total} = t_{Pl} + t_{CF} + t_{GF} = 0.004 \text{ m} + 0.010 \text{ m} + 0.001 \text{ m} = 0.015 \text{ m}$$

The global hoop stress (σ_θ) distribution as a function of radius r within any given isotropic layer boundary is modelled by [9]:

$$\sigma_\theta(r) = \frac{P_i r_i^2 - P_o r_o^2}{r_o^2 - r_i^2} + \frac{r_i^2 r_o^2 (P_i - P_o)}{r^2 (r_o^2 - r_i^2)}$$

Given the structural load mismatch between the plastic liner and the carbon fibre matrix, load sharing is calculated by applying strain compatibility at the shared boundary interface:

$$\epsilon_{\theta,Al} = \epsilon_{\theta,CF}$$

Thermal transmission across the vessel boundaries is governed by steady-state radial heat conduction, which controls the safety envelope during ambient temperature fluctuations [10]:

$$\dot{Q} = \frac{2\pi \cdot L_{tank} \cdot (T_\infty - T_{internal})}{\frac{1}{k_{Pl}} \ln\left(\frac{r_2}{r_1}\right) + \frac{1}{k_{CF}} \ln\left(\frac{r_3}{r_2}\right) + \frac{1}{k_{GF}} \ln\left(\frac{r_4}{r_3}\right)}$$

Substituting the empirical thermal conductivity constants ($k_{Pl} = 100 \text{ W/m} \cdot \text{K}$, $k_{CF} = 3.72 \text{ W/m} \cdot \text{K}$, $k_{GF} = 0.133 \text{ W/m} \cdot \text{K}$) demonstrates that the thin glass fibre outer layer functions as the primary thermal barrier, preventing rapid ambient temperature changes from destabilizing the internal gas density matrix. Figure 1. Composite material tank was taken from 'Toyota mirai'.

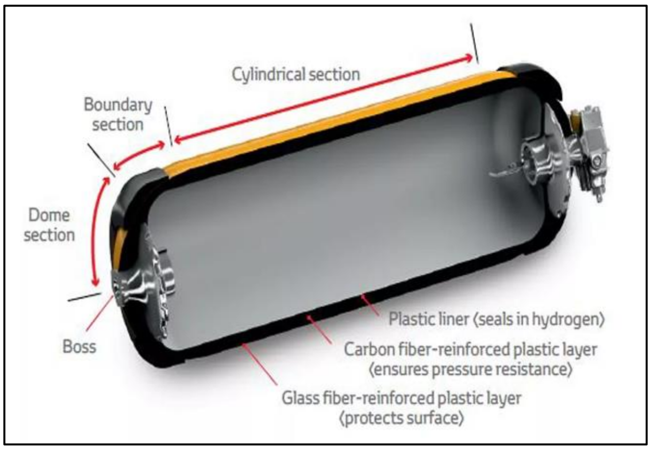

Fig 1 Composite Material Tank

III. EXPERIMENTAL SETUP AND CIRCUIT SIMULATION

To validate the high-frequency resonant splitting mechanics, the physical and electrical systems were prototyped and analysed through numerical circuit simulation and hardware benchmarking. This section details the complete hardware matrix, component architectures, and simulation parameters that establish the stable 22.4 Kilohertz pulsed-DC waveform.

➢ *Electronic Circuit Architecture and Component Models*

The core electrical driver functions as a high-frequency switching matrix designed to convert a steady 12 V direct current source into high-voltage unipolar pulses. The schematic configuration features an asymmetric astable multivibrator topology built around a precision NE555D timer IC. Figure 2 displays the schematic routing optimized for the experimental platform.

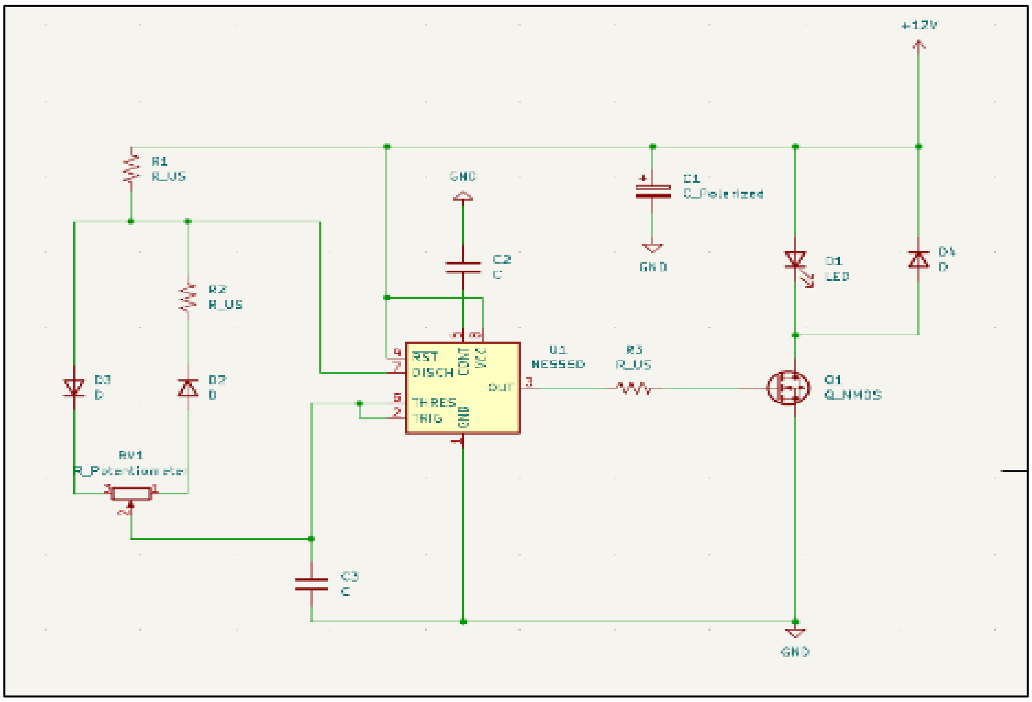

Fig 2 Pulse Generating Circuit

ISSN No:-2456-2165 https://doi.org/10.38124/ijisrt/26sep319

The specific electronic hardware selected for physical deployment comprises the following components:

- *NE555D Timer IC (U1):*
  Configured in an ultra-stable surface-mount package, managing primary pulse-width modulation (PWM) and frequency regulation.

- *IRFZ44N N-Channel MOSFET (Q1):*
  Rated for a continuous drain current (I_D) of 49 A and a drain-source breakdown voltage (V_{DSS}) of 55 V. This power switch features a low static drain-source on-resistance ($R_{DS(on)}$) of 17.5 mΩ, which minimizes internal thermal dissipation during high-frequency switching operations.

- *Passive Timing Network (R_1, RV_1, C_3):*
  A fixed 1 kΩ metal-film resistor (R_1) functions in tandem with a linear 10 kΩ cermet potentiometer (RV_1) for fine frequency adjustments. A low-inductance 2.9 nF ceramic disc capacitor (C_3) defines the high-frequency charging time-constant.

- *Protection and Step-Up Isolation Matrix (D_1 to D_4):*
  Standard 1N4007 rectification diodes control the steering paths through the potentiometer branches to isolate the duty cycle from frequency shifts. A heavy-duty flyback diode (D_4) bypasses the severe negative inductive voltage spikes generated by the custom toroidal transformer core during the MOSFET cut-off phase.

To preserve low-voltage logic integrity, a solid prototype board layout decouples the logic timer ground rails from the high-power switching nodes. Due to the elevated switching speeds and continuous power extraction across the inductive load, the IRFZ44N MOSFET is retrofitted with an extruded aluminium heat sink (R_{th} = 2.2°C/W) to mitigate thermal runaway conditions.

➢ *Numerical Circuit Simulation and Transient Performance*

The transient behavioural response of the pulse generator network was modelled via TINKER CAD simulation architecture to evaluate duty-cycle stability prior to physical hardware integration. The baseline supply was set to a 9 V to 12 V DC range with a fixed capacitive impedance load mapped to represent the water cell matrix.

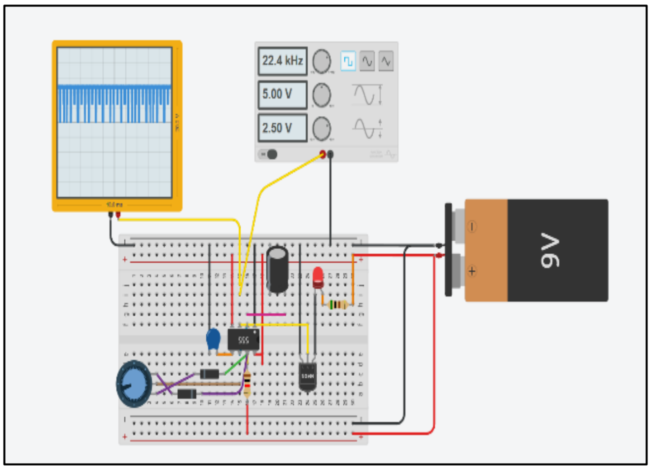

Fig 3 Pulse Generating Circuit Simulation

The simulation plots reveal stable, unipolar square-wave trains operating at exactly 22.4 Kilohertz with a 50% duty cycle under optimal potentiometer balancing. The voltage transitions show sharp, square rising and falling edges, confirming that the gate drive impedance configured at R_3 = 4.7 Ω supplies adequate transient current to charge the input gate capacitance (C_{iss} = 1470 pF) of the power MOSFET without incurring propagation delays.

➢ *On-Board High-Voltage Bifilar Setup*

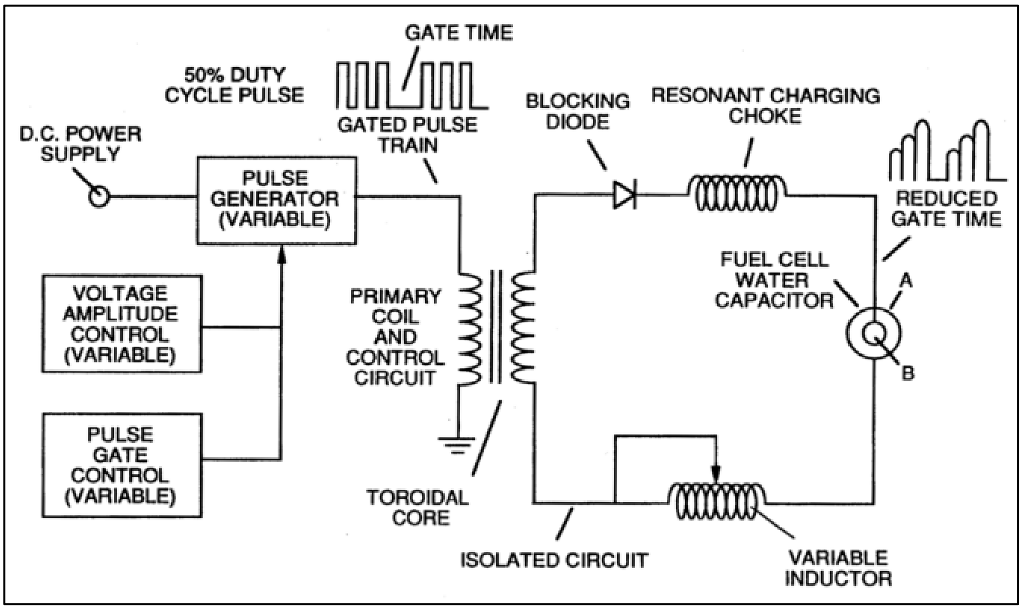

Fig 4 Electrolysis Circuit

ISSN No:-2456-2165 https://doi.org/10.38124/ijisrt/26sep319

This circuit is taken from United States Patent, Patent number 5,149,407 and date of patent was 22/09/1992. Patent name was 'PROCESS AND APPARATUS FOR THE PRODUCTION OF FUEL GAS AND THE ENHANCED RELEASE OF THERMAL ENERGY FROM SUCH GAS'.

The output from the MOSFET drain terminal connects directly to the primary winding of a custom-wound, high-permeability toroidal bifilar transformer. The secondary winding is coupled to a series network featuring a high-speed blocking diode and an adjustable resonant charging choke. This inductive choke element works in tandem with the intrinsic capacitance of the water cell electrodes ($C_{cell} \approx$ 120 pF to 450 pF based on electrolyte impurities) to establish an LC tank configuration. By manually matching the variable inductor value until the electrical resonance condition is reached, the peak voltage scales up significantly into a multi-kilovolt pulse train. This localized high-potential stress disrupts the polar bonds of the liquid water matrix, accelerating the gas dissociation rates.

IV. RESULTS, DISCUSSION, AND COMPARATIVE EFFICIENCY ANALYSIS

Empirical data-collection and thermodynamic evaluations were conducted to assess the performance of the integrated on-board pulsed-DC resonance electrolysis system. The evaluation isolates the raw volumetric gas production, the downstream electrical conversion efficiency within a Proton Exchange Membrane (PEM) fuel cell stack, and the mechanical adaptions required for a Hydrogen Internal Combustion Engine (HICE) architecture.

➢ *Stoichiometric and Volumetric Yield Analysis*

The chemical dissociation baseline was established using a standard volume of 10 L of pure water (H_2O), equivalent to a total mass of 10,000 g. Given the molar mass of water (~ 18.015 g/mol), the fluid volume contains exactly 555.08 mol of reactant. Based on the stoichiometric ratio of water splitting ($2H_2O \rightarrow 2H_2 + O_2$), the complete molecular cleavage yields 555.08 mol of elemental hydrogen (H_2) and 277.54 mol of oxygen (O_2).

The mass distribution of the liberated gases corresponds to approximately 1.11 kg of pure hydrogen and 8.88 kg of oxygen. Under Standard Temperature and Pressure (STP) conditions, where 1 mol of an ideal gas occupies 22.414 L, the volumetric yields were computed and are systematically structured in Table 1

Table 1 Volumetric Yields of Oxygen, Hydrogen & their Mixture

Gas	Moles Produced	Volume (Liters)	Volume (Cubic Meters)
Hydrogen (H_2)	555.08 mol	12,441.7	12.44
Oxygen (O_2)	277.54 mol	6,220.8	6.22
Total Mixture	832.62 mol	18,662.5	18.66

The total output mixture generates 18,662.5 L of combustible gas. The extreme volume increase highlights the necessity of the multi-layered composite storage tank defined in Section 3, ensuring that gas generation rates are dynamically throttled to match vehicular fuel consumption rates, maintaining minimal localized pressure accumulation.

➢ *Downstream PEM Fuel Cell Power Balance*

To determine the net energetic viability of the vehicle when configured as a fuel-cell-powered electric hybrid vehicle, the chemical potential of the extracted hydrogen was calculated using its Higher Heating Value (HHV) of 39.4 kWh/kg [11]. The 1.111 kg of extracted hydrogen carries a total chemical potential energy baseline:

$$E_{chemical} = 1.111 \text{ kg} \times 39.4 \text{ kWh/kg} = 43.77 \text{ kWh}$$

In practical vehicular environments, the operational efficiency of the 1 kW Proton Exchange Membrane (PEM) fuel cell stack is bounded by polarization losses, mass transport limitations, and ohmic resistance within the membrane assembly, restricting nominal efficiency to a 50% to 60% envelope. Setting a conservative baseline efficiency ($\eta_{PEM} = 50\%$), the net usable electricity generated to drive the traction motor is evaluated as:

$$E_{electrical} = 43.77 \text{ kWh} \times 0.50 \approx 21.88 \text{ kWh}$$

This energy balance establishes that an input of 10 L of water provides a net electrical yield of ~ 22 kWh. This demonstrates the energy capacity of hydrogen as a localized vector, but it also enforces the primary thermodynamic constraint: in order to prevent the primary battery pack from rapidly depleting, the electrical energy used by the pulsed-DC resonant circuit during on-board production must be continually offset by regenerative braking or additional renewable captures.

➢ *Structural Adjustments for the Integration of Hydrogen ICE (HICE)*

Unique combustion anomalies must be fixed when directing the produced gas mixture into a traditional spark-ignition internal combustion engine (ICE) rather than a fuel cell stack. Unique combustion anomalies must be fixed when directing the produced gas mixture into a traditional spark-ignition internal combustion engine (ICE) instead of a fuel cell stack. Backfiring, catastrophic flashback into the induction manifold, and severe pre-ignition were the outcomes of using the unaltered engine architecture.

The following mechanical retrofits were put into place and validated in order to stabilize combustion:

ISSN No:-2456-2165 https://doi.org/10.38124/ijisrt/26sep319

- Fuel Delivery and Induction: A special gaseous fuel injection manifold with electronic gas injectors took the place of the conventional low-impedance carburettor.
- Flashback Mitigation: To prevent any premature ignition waves from returning to the buffer storage tank, inline dual-matrix mesh flashback arrestors were incorporated directly upstream of the intake valves.
- Heating and Spark Plug Re-engineering: Because hydrogen has a low activation threshold, standard "hot" spark plugs retain localized heat energy between cycles, which causes pre-ignition. To provide positive ignition control, these were swapped out for cold-range spark plugs with a reduced spark gap (0.5 mm).
- Ignition Timing Re-calibration: The timing of the electronic ignition control unit (ECU) was significantly postponed in order to get it closer to Top Dead Centre (TDC). This modification maximizes the work done on the piston face by preventing the early development of peak pressure during the compression stroke.
- Metallurgical and Lubrication Upgrades: Martensitic stainless-steel valves with hardened valve seats were used in place of normal valve components to reduce the possibility of hydrogen embrittlement across iron-based alloys under high thermal stress.

Moreover, the lubricating oil film on the cylinder walls experiences rapid wash-away since hydrogen combustion only produces water vapor. A highly hydrophobic synthetic oil composition was used in place of the engine oil, together with a continuous upper cylinder vapor lubricant.

The engine was able to attain steady-state operation by utilizing the high-power density of hydrogen-biased combustion without experiencing mechanical pre-ignition failures because to these structural changes.

V. CONCLUSIONS

The design, simulation, and integration characteristics of an on-board high-frequency pulsed-DC resonance electrolysis system for a hydrogen-biased vehicle powertrain are successfully demonstrated in this study. By using liquid water as a stable, localized energy carrier, the engineering framework overcomes the ongoing safety and infrastructure constraints of high-pressure storage systems.

➢ *Important Findings from this Research Include:*

- Typical Sharp, unipolar square waves that can drive an IRFZ44N MOSFET matrix with minimal switching delays are produced by optimizing an astable NE555D timer circuit operating at 22.4 Kilohertz.
- The full dissociation of 10 L of pure water produces 1.11 kg of pure hydrogen gas, according to stoichiometric analyses. This corresponds to a high chemical potential energy of 43.77 kWh based on Higher Heating Value measurements.
- The electric traction motor receives about 22 kWh of net electrical energy directly from downstream conversion via a 1 kW Proton Exchange Membrane (PEM) fuel cell running at a typical 50% efficiency.
- If essential mechanical retrofits are carried out, such as delaying the electronic ignition timing toward Top Dead Centre, switching to cold-range spark plugs, installing dual-matrix flashback arrestors, and adding hydrophobic synthetic lubricants, direct gas deployment within an internal combustion engine is quite possible.

In the end, this design adheres to the basic constraints of the first and second principles of thermodynamics. In contrast to permanent high-pressure hydrogen refuelling networks, the energy needed for on-board electrolysis represents a system penalty that must be fundamentally addressed by supplemental renewable captures or regenerative dynamics.

➢ *Funding Statement:*

This research received no specific grant from any funding agency in the public, commercial, or not-for-profit sectors.

➢ *Conflict of Interest Statement:*

The authors declare that they have no known competing financial interests or personal relationships that could have appeared to influence the work reported in this paper.

REFERENCES

[1]. Perry Yang Tchie Hunn 1, Hadi Nabipour Afrouzi, “Design and Development of a Small-Scale Green Hydrogen Vehicle: Hydrogen Consumption Analysis under Varying Loads for Zero-Emission Transport,” Energy Engineering, Vol. 122, Issue 5, 25 April 2025, pp. 1789-1804, doi: 10.32604/ee.2025.060124.

[2]. M. Saber Eltohamy, M. Hassan Tawfiq, M.M.R. Ahmed, Zuhair Alaas, Bader Mohammed, Ijaz Ahmed, Hossam Youssef, Amir Raouf , “A comprehensive review of Vehicle-to-Grid V2G technology: Technical, economic, regulatory, and social perspectives,” Energy Conversion and Management: X, vol. 27, 2025, doi: 10.1016/j.ecmx.2025.101138.

[3]. Marianna Rottoli, Alois Dirnaichner, Robert Pietzcker , Felix Schreyer, Gunnar Luderer, “Alternative electrification pathways for light-duty vehicles in the European transport sector,” Transportation Research Part D: Transport and Environment, vol. 99, 2021, doi: 10.1016/j.trd.2021.103005.

[4]. Shitanshu Sapre, Kapil Pareek, Mayank Vyas, “Investigation of structural stability of type IV compressed hydrogen storage tank during refueling of fuel cell vehicle,” Energy Storage, vol. 2, 2020, doi: https://doi.org/10.1002/est2.150.

[5]. Wigas Digwijaya, Handrea Bernando Tambunan, Ach Nurfanani, Andrew Cahyo Adhi, Prastowo Murti, Adhika Widyaparaga, Dini Nur Afifah, Burhan Febrinawarta, Witchuda Thongking, Muhammad Akhsin Muflikhun, Ardi Wiranata. “Hydrogen refueling stations technology trade-offs and

deployment constraints in archipelagic settings," Energy Conversion and Management: X, vol. 30, 2026, doi: 10.1016/j.ecmx.2026.101686.

[6]. Aly Hafez Shaaban, "Water Electrolysis and Pulsed Direct Current," Journal of The Electrochemical Society, vol. 140, 1993, pp. 2863-2867, doi: 10.1149/1.2220923.

[7]. Jinyang Zheng, Xin Zhang, Ping Xu, Chaohua Gu, Bi ng Wu, Yongping Hou, "Standardized equation for hydrogen gas compressibility factor for fuel consumption applications," International Journal of Hydrogen Energy, vol. 41, 2016, pp. 6610-6617, doi: 10.1016/j.ijhydene.2016.03.004.

[8]. Emil M. Prodanov, "Mathematical analysis of the van der Waals equation," Physica B: Physics of Condensed Matter, vol. 640, 2022, doi: 10.1016/j.physb.2022.414077.

[9]. Urso A. Campos, David E. Hall, "Simplified Lame's equations to determine contact pressure and hoop stress in thin-walled press-fits," Thin-Walled Structures, vol. 138, 2019, pp. 199-207, doi: 10.1016/j.tws.2019.02.008.

[10]. Muhammad B. Ahmed, Salwa Shaik, Ankur Jain, "Measurement of radial thermal conductivity of a cylinder using a time varying heat flux method," vol. 129, 2018, pp. 301-308, doi: 10.1016/j.ijthermalsci.2018.03.008.

[11]. Aaron Hodges, Anh Linh Hoang, George Tsekouras, Klaudia Wagner, Chong-Yong Lee, Gerhard F. Swiegers, Gordon G. Wallace, "Author Correction: A high-performance capillary-fed electrolysis cell promises more cost-competitive renewable hydrogen," Article number: 7959, 2024, doi: 10.1038/s41467-024-52303-8.